Volume 1 | Number 1 | Jan 2013 | Pages 1–100

Journal of
Materials Chemistry A

Materials for energy and sustainability
www.rsc.org/materialsA

Li⁺

e⁻

ROYAL SOCIETY
OF CHEMISTRY

ROYAL SOCIETY
OF CHEMISTRY

www.rsc.org/materialsA

Journal of Materials Chemistry A

ARTICLE

A simplified theoretical guideline for overall water splitting using photocatalyst particles

Angel T. Garcia-Esparza and Kazuhiro Takanabe

Particulate photocatalytic water splitting is the most disruptive and competitive solution for the direct production of solar fuels. Despite more than four decades of work in the field of photocatalysis using powder semiconductors decorated with catalyst particles, there is no clear consensus on the factors limiting the solar-to-hydrogen efficiency (STH). To understand the intrinsic limitations of the system, we numerically simulated simplified two-dimensional photocatalytic models using classical semiconductor device equations. This work presents the sensitivity of quantum efficiency (QE) to the various semiconductor properties, such as absorption properties and carrier mobilities, and to the dispersion of catalyst particles, which create heterojunctions, the driving force for charge separation. As a result, a pinch-off effect was prevalent underneath the hydrogen evolution site, suggesting an undesired energetic barrier for electron diffusion to the catalyst. The simulation using the values reported in the literature revealed that the QE was exclusively governed by recombination in the bulk of the photocatalyst particles, hindering the charge separation efficiency before reaching the catalysts on the surface. Using some of the reported parameters, our simulation shows that a typical defective n-type semiconductor particle (~100 nm) ideally exhibits a QE of <5% in the visible light range per particle, which reaches only approximately 10% in a slurry after 4 consecutive absorbing units (1.4% STH, from simulated solar irradiation). Although the present model contains rigid limitations, we use these trends as an initial guideline to pursue a photocatalysis by design strategy, which may result in possible alternatives to achieve higher efficiencies.

Introduction

Harvesting energy from the sun directly in the form of chemical bonds represents the ultimate goal to sustain our exponentially growing society. In this respect, heterogeneous particulate photocatalytic overall water splitting is one of the most promising systems for sustainable and competitive solar hydrogen generation from an economic point of view.[1] For more than five decades, the development of an efficient artificial photosynthesis process has remained elusive.[2] The process has evolved from the inception of the first photoelectrochemical cells[3] to the development of so-called microphotoelectrochemical cells (i.e., photocatalytic slurry reactors);[4] however, the technology is still far from industrial commercialization. TiO$_2$ has been one of the most studied photocatalysts for many decades, yet it does not absorb 85% of the usable photons for water splitting available in the solar spectrum (≥1.6 eV).[5,6] Additionally, no clear understanding nor description of the chemical physics of charge separation and transport has been clearly developed from the work done with TiO$_2$.

Many photocatalytic systems in the literature have followed a thermal catalysis structure design of supported metal sites dispersed on the surface of, most frequently, an inert support.[7] One of the main differences between heterogeneous thermal catalysis and photocatalysis is that the semiconductor absorber is an essential active component. Light absorption introduces the first limiting step to the overall system, and the liquid phase environment influences the active component under illumination.[8] Photonic charge generation can intrinsically determine the overall efficiency of the photocatalytic system. Increasing the amount of photocatalyst will not increase the rate of produced H$_2$ proportionally (as photon absorption saturates); thus, normalization of a photocatalytic rate of product formation by grams of material is meaningless when the photocatalytic efficiency or reactor/device photonic efficiency is the primary concern.[9]

Particulate photocatalytic water splitting represents an enormous challenge because it involves an extremely complex series of photophysical and electrocatalytic steps.[8,10] One way to tackle this challenge may be to divide the problems into components that can be examined separately. The first part is associated with semiconductor properties, such as light absorption with charge generation, separation and transport (1. Semiconductor).[11–13] Then, electrochemistry can be used to optimize the required active sites for electrocatalytic hydrogen and oxygen evolution reactions or any other targeted reactions (2. Electrocatalyst),[14] including mass transport of reactants and solution environment (pH, present ions, temperature, etc.).[15,16] Finally, the critical step is to design all the interfaces

Division of Physical Sciences and Engineering, KAUST Catalysis Center (KCC), King Abdullah University of Science and Technology (KAUST), 4700 KAUST, Thuwal, 23955-6900 (Saudi Arabia).
†Electronic Supplementary Information (ESI) available

This journal is © The Royal Society of Chemistry 20xx

J. Mater. Chem. A, 2015, **00**, 1-3 | **1**

(e.g., electrocatalyst-photocatalyst, electrolyte-photocatalyst) when coupling the independently optimized systems (3. Interface).[14,17–19] The electrocatalyst-semiconductor contact interface is essential for successful overall water splitting.[7–10]

Until recently, there was a weak consensus on how to evaluate and rigorously compare the efficiency of photocatalytic systems.[20] Different from the photovoltaic solar cell community, there are less consistent theoretical frameworks to describe the physicochemical behaviors of photocatalysts, particularly their charge carrier dynamics.[21–27] The fundamental physical phenomena at the semiconductor-electrolyte interface have been described in the literature, particularly detailed for photoelectrochemical electrodes.[27–29] Recent work provided a theoretical description of the experimental behavior of a Si photoelectrode covered with patterned nanoscale Ni catalysts under bias-control.[31] Rossi and Lewis used a point-dipole approximation, called the Tung model, for the simulation of the current-potential curve of such a photoelectrochemical cell working in a well-defined redox-potential electrolyte.[32] Furthermore, a recent study on the modelling and simulations of semiconductors coated with ion-permeable or dense electrocatalysts described the experimental results obtained from TiO_2 photoelectrodes coated with porous non-noble metal Ni oxyhydroxide catalysts.[33,34] Alternatively, other groups have provided a theoretical reference to model an Fe_2O_3 photoelectrode with a reasonable description of their current-potential behavior under typical experimental conditions found in the literature.[35,36]

Nevertheless, the study of models describing particulate photocatalysis is still limited and only few works can be found in the literature.[37–41] Hisatomi et al. recently reported numerical simulations of a so-called asymmetric one-dimensional photocatalytic model using $LaTiO_2N$ to understand the fundamental limiting factors of the semiconductor material.[42] However, it is still not possible to model powdered semiconductors and much less venture to predict quantum efficiencies for unbiased photocatalytic systems. Here, we use a finite-volume method to simulate two-dimensional particulate photocatalytic model systems decorated with metal nanoparticles on the surface of the semiconductor. We use the classical semiconductor equations to describe the electrostatics and charge carrier drift and diffusion, in an effort to understand the limitations of the photocatalytic technology. The aim is to humbly calculate reasonable trends to determine the maximum achievable solar-to-hydrogen conversion efficiency (STH) using a powder-form photocatalytic water splitting device.

Model

The simulations to solve the potential and current transport in particulate photocatalytic systems were performed using COMSOL Multiphysics. Table 1 provides the symbols of the parameters used in the models to calculate the semiconductor-catalyst, semiconductor-electrolyte interfaces. The numerical calculation uses a finite volume method

employing Scharfetter-Gummel discretization for particle transport. In COMSOL, the current is implicitly conserved using this method. The model entails numerically solving the semiconductor equations consisting of the Poisson's equation and the current continuity equations for each charge carrier (Equations 1-3).[43,44]

Table 1. List of symbols and abbreviations.

Symbol	Unit	Description
q	C	elementary charge
k_B	J K^{-1}	Boltzmann constant
h	J s	Planck constant
T	K	temperature
ε_0	F m^{-1}	vacuum permittivity
ε_r		relative permittivity
ϕ	V	electrostatic potential
E	V m^{-1}	electric field
n, p	m^{-3}	electron and hole concentration
n_i	m^{-3}	intrinsic carrier concentration
n_0, p_0	m^{-3}	quasi-equilibrium carrier density
N_D, N_A	m^{-3}	donor and acceptor density
N_C, N_V	m^{-3}	effective density of states in the conduction and valence band
J_n, J_p	A m^{-2}	electron and hole current density
U_n, U_p	m^{-3} s^{-1}	net electron and hole recombination rate
G_n, G_p	m^{-3} s^{-1}	electron and hole generation rate
R_n, R_p	m^{-3} s^{-1}	electron and hole recombination rate
D_n, D_p	m^2 s^{-1}	electron and hole diffusion constant
μ_n, μ_p	m^2 V^{-1} s^{-1}	electron and hole mobility
τ_n, τ_p	s	electron and hole lifetime
τ_c	s	collision time
P_0	m^2 s^{-1}	photons absorbed from AM 1.5G
α	m^{-1}	absorption coefficient
x	m	depth into the bulk of a semiconductor
ρ	m	surface of the semiconductor
r_0, r_s	m	catalyst and semiconductor particle size (diameter)
θ	rad	angle defining interparticle distance
x_d	m	depletion layer width
χ	eV	semiconductor electron affinity
Φ_B	eV	emission barrier height
E_g	eV	band gap
E_{ox}	eV	standard water oxidation energy
E_f	eV	semiconductor Fermi level
E_{fm}	eV	metal Fermi level
E_{fn}, E_{fp}	eV	quasi-Fermi level of electrons and holes
E_C	eV	conduction band edge
E_V	eV	valence band edge
m_e	kg	electron mass
$m^*_{n, p}$		effective electron and hole mass
$A^*_{n, p}$	A m^{-2} K^{-2}	effective Richardson constant for

electrons and holes

$$\nabla \cdot (\nabla \phi) = -\frac{q}{\varepsilon_0 \varepsilon_r}(p - n + N_D - N_A) \qquad (1)$$

$$\frac{\partial n}{\partial t} = -\frac{1}{q}\nabla \cdot J_n - U_n \qquad (2)$$

$$\frac{\partial p}{\partial t} = \frac{1}{q}\nabla \cdot J_p - U_p \qquad (3)$$

Electron and hole currents are defined using the general drift-diffusion equations (Equations 4-5).

$$J_n = q\left(\mu_n n E + D_n \nabla n\right) \qquad (4)$$

$$J_p = q\left(\mu_p p E - D_p \nabla p\right) \qquad (5)$$

$$E = -\nabla \phi \qquad (6)$$

The net recombination rate U in Equations 2 and 3 is calculated from the generation G and recombination R mechanisms in the model.

$$U_{n,p} = \sum R_{n,p,i} - \sum G_{n,p,i} \qquad (7)$$

The generation rate term assumes generation of one exciton (electron-hole pair) for each photon absorbed at any point in the semiconductor model (Equation 5). Using Lambert-Beer's law, without considering reflection and scattering events, the absorption of light depends on the absorption coefficient α of the material and its thickness x.

$$G_n = G_p = P_0 \alpha e^{(-\alpha x)} \qquad (8)$$

The photon flux density P_0 is the integration of the incident photons in the AM 1.5G solar spectrum (1000 W m^{-2}) with energies larger than the semiconductor's band gap. The created electron-hole pairs must be separated into free excited carriers for subsequent transfer to the surface where they may catalyze redox reactions. The mobility and the diffusion of free electrons and holes in the semiconductor are described through the Einstein relations.

$$D = \frac{k_B T}{q}\mu \qquad (9)$$

$$\mu = q\frac{\tau_c}{m^*} \qquad (10)$$

Excited conduction band electrons and valence band holes may recombine by traps. Here, the calculation assumes only a defect-assisted recombination type of process called steady-state Shockley-Read-Hall recombination.[44]

$$R_n = R_p = \frac{np - n_i^2}{\tau_p\left(n + N_C e^{-\frac{E_C - E_t}{k_B T}}\right) + \tau_n\left(p + N_V e^{\frac{E_V - E_t}{k_B T}}\right)} \qquad (11)$$

An ideal and simplified Schottky interface was assumed to calculate the current in the electrolyte-semiconductor interface as

$$\mathbf{n} \cdot J_n = -qv_n(n - n_0) \qquad (12)$$

$$\mathbf{n} \cdot J_p = qv_p(p - p_0) \qquad (13)$$

$$n_0 = N_C e^{\left(\frac{E_C - E_{fm}}{k_B T}\right)} = N_C e^{\left(\frac{\Phi_B}{k_B T}\right)} \qquad (14)$$

$$p_0 = N_V e^{\left(\frac{E_{fm} - E_V}{k_B T}\right)} = N_V e^{\left(\frac{E_g - \Phi_B}{k_B T}\right)} \qquad (15)$$

$$\Phi_B = E_{ox} - \chi \qquad (16)$$

In Equation 12 and 13, $\mathbf{n}$ represents an outward oriented vector normal to the boundary. This assumption treats the rectifying contact as a sink for carriers with specific recombination velocities v_n and v_p:

$$v_n = \frac{A_n^* T^2}{qN_C} \qquad (17)$$

$$v_p = \frac{A_p^* T^2}{qN_V} \qquad (18)$$

$$A_{n,p}^* = 4\pi m_{n,p}^* q k_B^2 h^{-3} \qquad (19)$$

Figure 1 shows the geometrical models used to approximate the electrostatics and carrier dynamics of a particulate semiconductor decorated with a metallic catalyst on its surface. The ρ-direction symbolizes the semiconductor surface, x-direction represents the distance from the surface interface into the bulk or it can be understood as the size of the semiconductor particle, r_0 represents the diameter size of the metallic catalyst particle, and the angle θ controls the interparticle distance of the catalysts distributed on the surface of the semiconductor in Model IV. The geometric models were discretized using free-triangular elements. The minimum element size was restricted to 8×10^{-12} m with a growing rate with a maximum element size of 4×10^{-10}. To solve for the large curvatures and steep gradients in the potential and/or carrier concentration, the mesh spacing is finest at the semiconductor interface with either Schottky or Ohmic junctions (Figure S1).

In Figure 1, Models I and II show two of the simplest box-type models for a semiconductor photocatalyst in contact with an electrolyte and a single or multiple metallic catalysts on its surface. The electrolyte-semiconductor interface and the metal-semiconductor contact were considered to be a Schottky junction in Model I. Dirichlet and Neumann boundary conditions were used in the models. The potential and the gradient changes for Models I and II and the flux of charges in

Model III were considered to be negligible when using a suitable scale for the box model (i.e., when the x magnitude is much larger than the depletion layer x_d, then we assumed that $\phi = \nabla\phi = \mathbf{n}\cdot J_n = \mathbf{n}\cdot J_p = \mathbf{n}\cdot D = 0$).
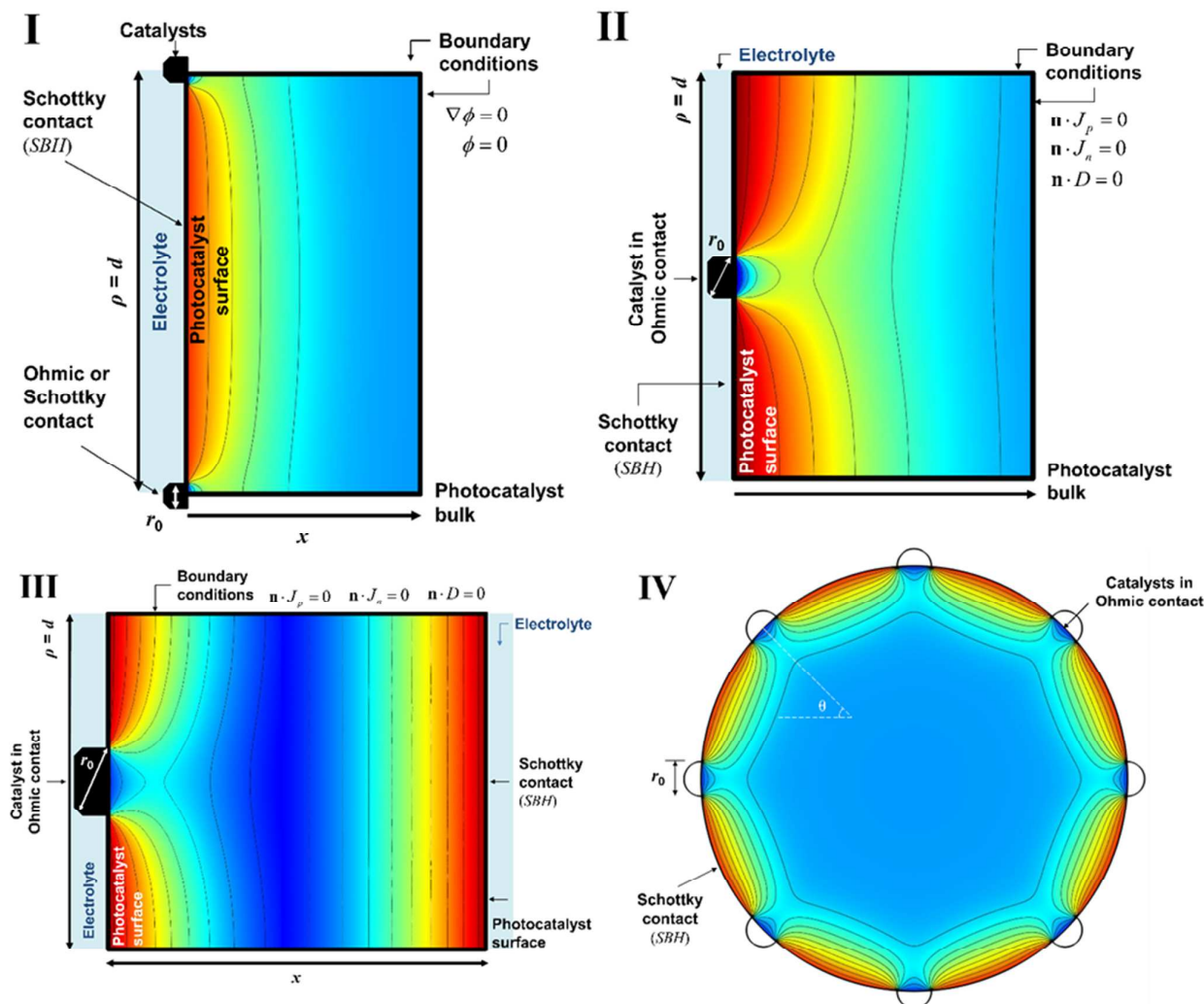
Fig. 1 Geometric model schemes with the boundary conditions and the assumptions used for the simulations. The *x*-direction represents the distance into the bulk of the semiconductor. The *ρ*-direction represents a position on the surface of the *n*-type model. Model I presents the box-type model used to calculate the equilibrium conditions in the dark for inhomogeneous Schottky contacts. Steady-state illumination conditions are assumed to calculate Models II-IV. Model II describes a single metal site surrounded by the electrolyte. Model III represents a similar geometry considering an electrolyte interface on both sides (left and right). Model IV shows a 100-nm spherical semiconductor particle decorated with metal catalysts. The θ variable is used to control the interparticle distance. We assumed an Ohmic junction for the metal catalysts in contact with the semiconductor for Models II-IV, whereas a Schottky contact was assumed to calculate the electrolyte interface for all models.

Periodic conditions can be used to extrapolate the equipotential profile results along the *ρ*-axis in Models I, II and III. Note that Model III considers an electrolyte interface on both sides along the *x*-direction. Model IV represents a spherical semiconductor particle with multiple hemispherical metallic catalysts on its surface. Sunlight irradiation was assumed incident to the models in the *x*-direction from left to right. Shadowing or scattering events arising from the metallic sites in the surface were ignored for the current calculations.

The starting premise is that the surface is under steady-state conditions for redox reactions under illumination; hence, the redox potentials were defined as the working potentials for the hydrogen evolution reaction (HER) and oxygen evolution reaction (OER). For simplicity, the assumption implicates a rather ideal situation where the photocatalyst device is under illumination in steady-state overall water splitting conditions. All these models assume that the electrolyte interface forms a depletion layer with the *n*-type

semiconductor, generating band bending in a Schottky-type junction.[30] A steady-state standard overpotential of 300 mV was set for water oxidation, whereas no overpotential was considered for hydrogen production. Here, the metal catalyst is at the standard potential for the HER and forms an Ohmic contact with the semiconductor for Models II, III and IV. In the following sentences, we will explain the basis of this critical assumption. During steady-state overall water splitting, the cathodic active site must be at least at the standard potential to generate hydrogen gas (4.44 eV),[35,36] and its partial pressure near the site can be large, affecting the redox potential in such negatively charged site and possibly forming an Ohmic junction.[45,46] For the calculations we assumed that exited electrons in the conduction band transfer directly to the active site already with the required potential for HER through an Ohmic-type junction. These assumptions lead to the metallic catalyst being the active site for HER, while the semiconductor surface is the active site for the OER under steady-state illumination conditions (Figures 5-8).[8,45–47] Table 2 presents the material parameters used in the simulations unless otherwise stated.

Table 2. List of semiconductor material parameters required for the numerical simulations. The values of Ta_3N_5 are used as a starting point, but not limited to.

Symbol	Value	Unit
q	1.602×10^{-19}	C
k_B	1.3806×10^{-23}	J K^{-1}
h	6.626×10^{-34}	J s
m_e	9.11×10^{-31}	kg
T	300	K
ε_0	8.854×10^{-12}	F m^{-1}
ε_r	17	
μ_n, μ_p	2×10^{-4} [a]	m^2 V^{-1} s^{-1}
τ_n, τ_p	5×10^{-12} [a]	s
P_0	7×10^{20} [b]	m^2 s^{-1}
α_{550}	6.1×10^6	m^{-1}
x	1×10^{-7}	m
ρ	2×10^{-8}	m
r_0	8×10^{-9}	m
r_s	1×10^{-7}	m
χ	4.3	eV
E_g	2.1	eV
E_{ox}	5.97	eV
m^*_n	1.9 [a]	
m^*_p	3.4 [a]	
N_C	6.3×10^{25} [c]	m^{-3}
N_V	1.5×10^{26} [c]	m^{-3}
A^*_n	2.3×10^6 [c]	A m^{-2} K^{-2}
A^*_p	4.1×10^6 [c]	A m^{-2} K^{-2}

[a] values obtained from reference 12.
[b] integrated photons from 300 < λ < 550 nm in AM 1.5G.
[c] calculated value from effective mass.

Model I in Figure 1 was used to solve for the equilibrium conditions in the dark, and the simulation results are

presented in Figures 3 and 4. Model II, III and IV were solved under the assumption of steady-state illumination, and the results are present in Figures 5-8. The results of this work will be presented with increasing complexity of the model and the simulation. We start by analyzing only the implications of the absorption properties of the semiconductor in function of the defect density in *n*-type materials (Figure 2). Then, we solve for the potential under equilibrium conditions in the dark to understand the apparent driving force for drift and diffusion of charges (Figure 3 and 4). Later, we introduce simulated steady-state solar radiation to study charge transport. The purpose of the study is to obtain quantum efficiency (QE) trends of the models by perturbing the different semiconductor parameters. Moreover, we will explore the effects of the catalyst size and the interparticle distance in the QE (Figures 5-8).

We used the Ta_3N_5 properties as a starting point in our investigation because recent literature produced a thorough characterization of the material.[12,13,17,19] The results presented hereafter, however, may well represent any semiconductor material with the parameters described in the calculation details. Our aim in this study was to test the typical photocatalysis configuration to explore what is possible to achieve in terms of efficiency and what we can learn from these idealized conditions. It is important to understand the idealized conditions for charge generation, separation and transport in photocatalysis before exploring more complete and complicated models. The calculations do not consider surface states, potential determining ions on the surface, inhomogeneous doping profiles, other recombination mechanisms than trap-assisted recombination, and additional potential losses from kinetics and mass transport. The simulations presented refer to only one semiconductor particle in the particulate system. An important point to consider is that we will first discuss calculations for a single absorbing unit (Figure 5-8), and later we estimate an accumulated efficiency in the photocatalytic slurry (Figure 7B and 8B).

Results and discussion

$$W_d = \sqrt{\frac{2\varepsilon_0\varepsilon_r|V_{bi}|}{qN_D}} \tag{20}$$

Equation 20 was obtained using the full depletion approximation to solve the one-dimensional Poisson equation.[27,36] This equation describes the magnitude of the depletion layer W_d as a function of the defect density in the semiconductor N_D, the potential difference across the semiconductor, which equals the built-in potential V_{bi} generated at the Schottky interface, and the relative dielectric constant of the semiconductor ε_r. Powder form photocatalysts are, in general, highly defective semiconductors with high carrier densities on the order of $>10^{18}$ cm^{-3}.[17,48] Figure 2A shows the effect of the donor density on the magnitude of the depletion width obtained using Equation 20 (*n*-type semiconductor case). Based on the assumption of a 1 V built-in

potential, we can estimate a very narrow depletion space near the interface of less than 50 nm into the bulk of a semiconductor, using a dielectric constant of 17 measured experimentally at high frequency for Ta_3N_5.[12] For most semiconductors studied in the literature and based on this approximation, to achieve a depletion length larger than 100 nm, it is required to make *n*-type semiconductor crystals with donor densities on the order of $<10^{17}$ cm^{-3}. If we assume that the dielectric constant of the semiconductor is 1 order of magnitude larger,[13,49] the depletion length region roughly doubles in magnitude at similar donor densities (Figure S2). Nevertheless, to generate depletion regions larger than 100 nm, the crystal must possess a carrier density of less than 10^{18} cm^{-3} (Figure 2A). In particulate heterogeneous photocatalyst systems, charge separation only relies on the formation of an effective semiconductor-electrolyte Schottky type of contact, and the efficient diffusion of charge carriers.[8] The depletion layer may be described as a charge separation region that decays in space. Thus, Figure 2A provides a qualitative and quantitative expectation of this charge collection region into the semiconductor photocatalyst based on carrier density.
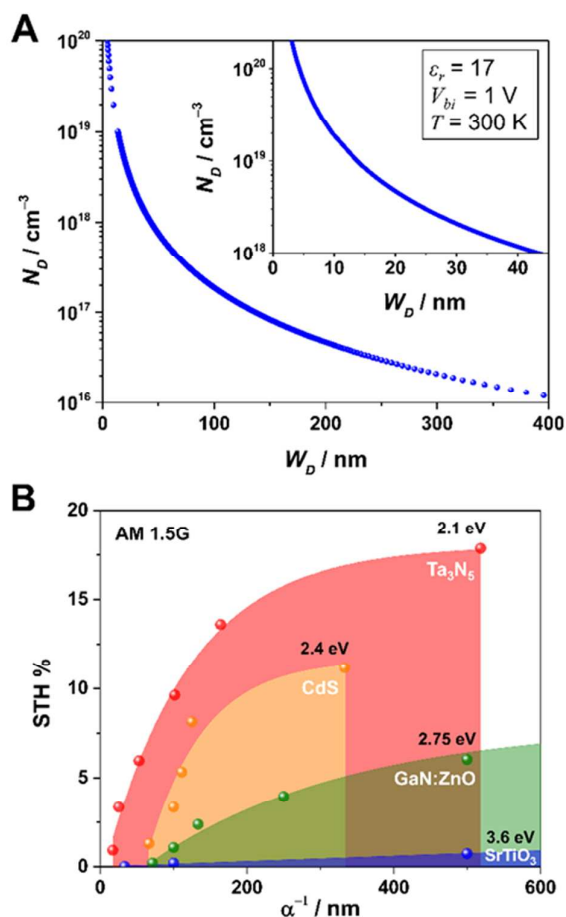
conversion efficiency as a function of the penetration depth of light. A 100% QE was assumed utilizing simulated solar radiation (AM 1.5G). The points in the Figure represent experimentally obtained absorption coefficients from the literature.[11–13,50–55]

To provide a complete idea of the implications of this charge collection layer, we analyzed the absorption properties of some semiconductor materials with the theoretical capability for overall water splitting.[1,7,10,48] All semiconductors used in Figure 2B have the required energetic conditions for water splitting. The band gaps are larger than 2 eV, and the valence and conduction bands are more positive than the standard water oxidation potential and more negative than the water reduction potential, respectively. Figure 2B shows the required absorption depth in a single semiconductor particle to absorb available photons in the solar spectrum and attenuate light by e^{-1} to generate enough charge carriers for hydrogen generation. The figure presents the maximum theoretical STH as a function of the inverse of the absorption coefficient (α). The calculation was performed assuming 100% QE and using the number of incident photons in AM 1.5G. The data points in Figure 2B represent experimentally measured absorption coefficients at different wavelengths,[11–13,50–55] where the inverse of this magnitude represents the penetration depth of the light into the semiconductor absorber. The absorption coefficient changes as a function of the photon wavelength; high energy photons are absorbed closer to the surface due to the high absorption coefficient of semiconductors at shorter wavelengths. $SrTiO_3$ is a large band gap semiconductor material, and similar to TiO_2 and ZnO, only capable of UV-light absorption, limiting its STH efficiency to a maximum of 1.5% while assuming perfect QE (Figure 2B). Therefore, the large band gap completely renders the semiconductor useless for solar energy applications as the benchmark target is, in general, set to 10% STH to make the technology competitive in the energy market.[8,20] The 10% STH target is generally applied to photoelectrochemical water splitting cells; nevertheless, particulate photocatalytic powders may become commercially viable if it is possible to achieve 5% STH.[1,56] Almost a decade ago, a GaN:ZnO solid solution with a supported mixed oxide of Rh and Cr on its surface was found to split water efficiently using visible light with a QE of 2.5% at 420-440 nm and less than 1% QE at wavelengths longer than 450 nm (E_g = 2.75 eV).[57] Assuming that it is possible to optimize the QE of this photocatalyst and based on the usable photons, we could expect to achieve only around half of the general benchmark target (i.e., 6% STH for GaN:ZnO in Figure 2B).

It should be emphasized that the primary factor to determine the efficiency originates from absorption properties. The use of visible light photons is critical for the practical development of large-scale solar energy conversion via photocatalysis, as can be seen from the achievable maximum STH efficiency due to the different bandgap of the materials shown in Figure 2B. To achieve the 10% target, we must turn to semiconductors with band gaps smaller than 2.4

Fig. 2 (A) Description of the depletion layer width with changing donor density assuming and built-in potential of 1 V in an *n*-type semiconductor material with a relative dielectric constant of 17 at 300 K. (B) Theoretical solar-to-hydrogen

6 | *J. Mater. Chem. A*, 2015, **00**, 1-3

This journal is © The Royal Society of Chemistry 2015

eV but, in general, larger than 1.8 eV for a single-absorber photocatalytic H_2 producing system (i.e., to account for overpotential losses). CdS and Ta_3N_5 are promising photocatalysts for overall water splitting with 2.4 eV and 2.1 eV band gaps and maximum theoretical STHs of 11% and 17.8%, respectively.[18,19] Based on the absorption properties, Ta_3N_5 particles with sizes on the order of 100 nm are transparent to 500-600-nm photons with an achievable theoretical STH of <10%. If the particle size is in the range of 50 nm, photons with wavelengths longer than 450 nm will not be absorbed by the particulate material, dropping the attainable STH efficiency to <6%. A 500-nm thickness of Ta_3N_5 particles is required for complete absorption of the usable photons in the solar spectrum to achieve the theoretical maximum efficiency for a 2.1 eV band gap semiconductor. A 100-nm CdS particle can produce <5% STH; hence, the semiconductor requires a minimum penetration depth of 300 nm to reach >10% STH. One of the advantages of particulate systems is the use of multiple absorbing entities dispersed in a solution to fully absorb incident light. The estimations presented in Figure 2B apply not only to single particles but also to thin film configurations. Until
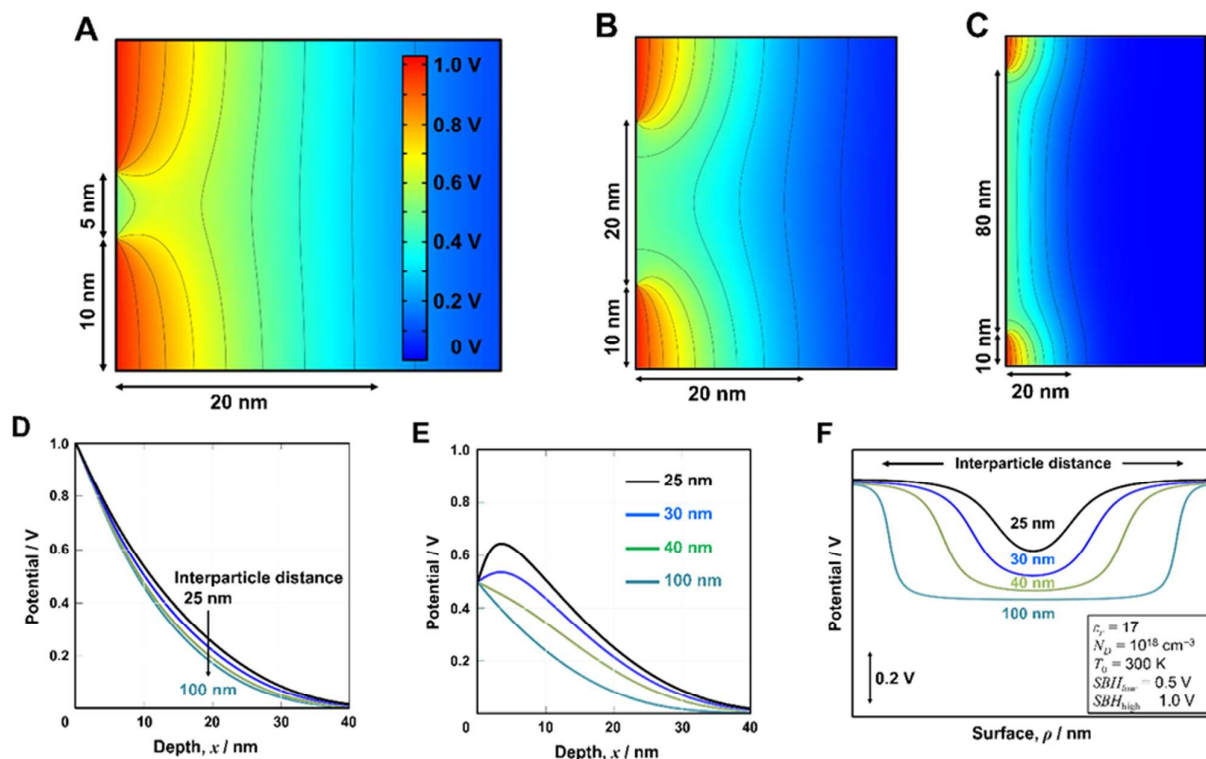
Fig. 3 Equilibrium-condition simulations for Model I. Inhomogeneous Schottky contacts with different magnitudes are used. The catalysts and the electrolyte are assumed to form a rectifying junction with the semiconductor. The metal sites have a Schottky barrier height of 1 V. The hypothetical electrolyte interface has a barrier height of 0.5 V. (A) The catalysts have an interparticle distance of 5 nm on the surface of the semiconductor. The interparticle distance increases to (B) 20 nm and (C) 80 nm. The size of the metal catalysts remains constant in all the figures (20 nm). Potential profiles are presented under the catalyst (D) and the electrolyte junctions (E) into the semiconductor bulk. The potential gradients at 2 nm under the surface (ρ-direction) are shown with changing scale while increasing the interparticle distance (F). The potentials are drawn from one catalyst particle to the other. The semiconductor properties used for the calculations are a donor density of 10^{18} cm^{-3}, a relative dielectric constant of 17 and a temperature of 300 K.

this point, we have discussed the absorption properties of semiconductors based solely on their optical band gaps. Figure 2 exhibits a relation between charge generation (Figure 2B) and charge separation (Figure 2A) using simple fundamental semiconductor properties. For example, Ta_3N_5 particles with donor densities greater than 10^{18} cm^{-3} generate a depletion layer on the order of tenths of nanometers (Figure 2A), nevertheless the amount of photons absorbed in this range is very limited (Figure 2B), substantially limiting the STH efficiency of the system (i.e., less than 5% STH assuming 100% QE). Systematic semiconductor characterizations and DFT calculations have shown that Ta_3N_5 efficiency may be limited by poor transport properties and fast carrier recombination.[12,13,17,19] Thus, it may be reasonable to assume that the probability of charge separation and transport beyond the space charge region at the interface would be small. That being said, longer wavelengths in the solar spectrum may be used if the quality of the semiconductor crystal is high.

Efficient charge separation requires long-range electric fields in the hundreds of nanometers range, comparable to the penetration depth of visible light in the semiconductor material.

The effects of inhomogeneous Schottky contacts have been previously studied by Tung and coworkers.[58] They modelled the case when a semiconductor-metal interface formed an inhomogeneous Schottky junction.[59] In this system, regions along the interface have Schottky barriers with different magnitudes. Tung used a point-dipole approximation

have been used to describe the electrostatic phenomena found in these types of contacts with results that are similar to Tung's approximation.[61] As a starting point to validate our model, we constructed one of Tung's models and compared our calculations with his results (Figure S3). Equipotential curves were obtained for a Si slab in contact with two regions exhibiting a different Schottky barrier height (SBH).[61] The obtained results are in reasonable agreement, and our model captures the characteristic pinch-off effect reported by Tung in inhomogeneous Schottky contacts.[59–61] Model I in Figure 1
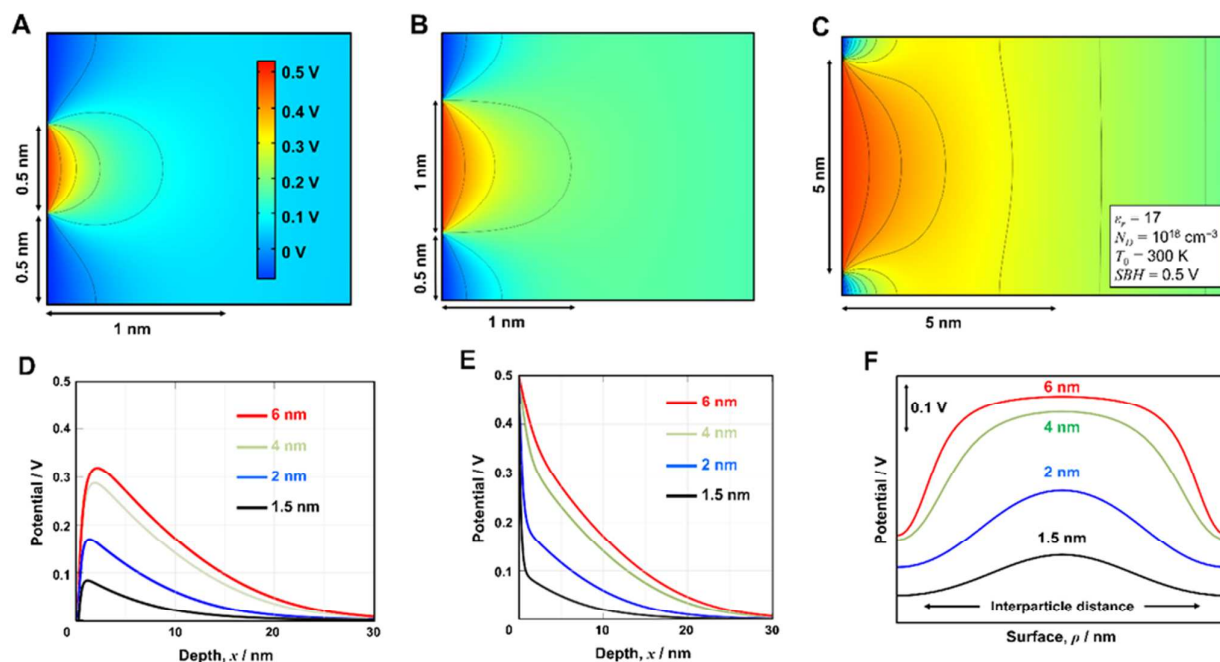
Fig. 4 Equilibrium-condition simulations for Model I where the catalysts are assumed in Ohmic contact with the semiconductor. The electrolyte is considered as a Schottky contact. The electrolyte interface has a barrier height of 0.5 V. (A) Two metallic sites are highly packed and separated by an interparticle distance of 0.5 nm. The catalysts size is 1 nm and remains constant in these calculations. The interparticle distance increases to (B) 1 nm and (C) 5 nm. (D) Potential profiles are presented under the catalyst, and (E) the electrolyte interfaces into the semiconductor bulk. (F) The potential gradients at 0.5 nm under the surface (ρ-direction) are shown with changing scale while increasing the interparticle distance. The potentials are drawn from one catalyst particle to the other. The semiconductor properties used for the calculations are a donor density of 10^{18} cm^{-3}, a relative dielectric constant of 17 and a temperature of 300 K.

represents the case where two catalysts on the surface of a semiconductor photocatalyst may form severe Schottky barriers. Let the Schottky contact with the electrolyte have a lower SBH than the one assumed for the metallic counterpart. Figure 3 shows the results obtained for a semiconductor with a relative dielectric constant of 17 and a donor density of 1×10^{18} cm^{-3} at 300 K. We placed two 20-nm metallic particles on its surface along the ρ-direction, forming a high SBH of 1.0 V, whereas the hypothetical electrolyte was assumed to produce an SBH of 0.5 V. Then, we proceeded to change the interparticle distance of the catalysts to study the effects of the potential gradients into the semiconductor as shown in Figure 3A, 3B and 3C. In agreement with the full depletion

approximation shown in Figure 1, the potential gradient was mostly lost 20 nm into the bulk of the semiconductor due to the high carrier density concentration. Figure 3A shows that the potential from the high SBH in the metallic contact extends under the semiconductor-electrolyte interface if the two metal particles are relatively close. When the interparticle distance of the metals is significant and the high SBH region is isolated on the semiconductor surface, the potential influence diminishes as observed from the color gradients in Figure 3B and 3C. The potential profile under the metal catalyst and under the electrolyte interface into the bulk of the semiconductor are presented in Figure 3D and 3E, respectively. The figures show the changes in the potential gradient with

changing interparticle distance. As observed from these results, the potential that develops under the surface was apparently affected by the high SBH region with changing interparticle distance (Figure 3E), whereas the effect under the high SBH contact was almost negligible (Figure 3D). The high SBH of 1.0 V produces the depletion region expected from an *n*-type semiconductor-metal Schottky contact. In contrast, a pinch-off effect was observed in the low SBH region of 0.5 V with decreasing interparticle distance. When the interparticle distance between the two metal particles is comparable to the size of these high SBH patches (ca. double or less), the potential gradient under the low barrier region was affected, producing an increase in the barrier height to approximately two-thirds of the magnitude of the higher SBH region (Figure 3E). The relative potential difference generated at the Schottky interface was lost 40 nm into the bulk (Figure 3D and 3E). The potential levels obtained from 20 Angstroms under the semiconductor's surface are presented in Figure 3F. The horizontal axis represents the surface of the semiconductor in the ρ-direction, and the colored signals represent changing scales with changing the interparticle distance of the metals on the surface. The relative potential magnitudes are represented on the vertical axis. When the metal catalysts are 100 nm apart, it is possible to find two well-defined potential levels. The high potential magnitude equals the high SBH value of 1.0 V under the metal catalyst. The lower potential magnitude in the center of Figure 3E represents the low SBH region under the electrolyte (i.e., 0.5 V). Our calculations resolve the potential gradient generated from the high potential region to the lower potential levels. The changing gradients observed in Figure 3E may represent the one-dimensional charge separation profile for photoexcited charge carriers near the surface. As the interparticle distance decreases to a similar order of magnitude as the high SBH region, the potential gradient decreases, most likely affecting charge separation. It follows that the observed potential wells provide qualitative evidence of the restricted regions for charge separation in a particulate semiconductor photocatalyst.

Now, let us assume that the metal catalysts on the surface are in Ohmic contact with the semiconductor particle (Model I, Figure 4). The semiconductor-electrolyte Schottky barrier height was assumed to be 0.5 V in this case. For these calculations, we used a donor density of 1×10^{18} cm^{-3}, a relative dielectric constant of 17 and temperature of 300 K. The effects of the potential gradients with changing interparticle distance of the non-rectifying metallic junctions were studied as shown in Figure 4A, 4B and 4C. Figure 4A shows two 1-nm metal particles on the surface of a semiconductor with an interparticle distance of 0.5 nm, thus exposing a very narrow region of the semiconductor surface to the electrolyte. It is interesting to note that, in regions where the metallic nanoparticles are highly packed, the potential gradient extends only a few nanometers into the bulk of the semiconductor (Figure 4A). As the nanoparticles become more isolated and are surrounded by large fractions of the electrolyte interface, some potential gradient effects start to become clear. Figure 4B and 4C show metal nanoparticles with interparticle

distances larger than the Ohmic junction. The results indicate that the equipotential profiles produced by the semiconductor-electrolyte interface extend well under the Ohmic junction (Figure 4B and 4C). As the interparticle distance increases, the depletion layer formed at the Schottky junction increases to a similar magnitude as observed in our previous calculation (ca. 30-40 nm, Figure 4D and 4E). In contrast, the Ohmic region under the metal nanoparticles decreases with increasing interparticle distance, extending less than 1 nm into the bulk under the metal contact (Figure 4B and 4C). In a similar manner, with decreasing interparticle distance, the potential gradient at the electrolyte interface in Figure 4A extends less than 1 nm before decreasing to less than 20% of the interface potential difference (Figure 4E, -1.5 nm- black signal). Figure 4D presents the potential gradients obtained under the nanoparticle contact along the *x*-direction into the bulk of the semiconductor with changing interparticle distance. By definition, we consider a junction to be Ohmic when the SBH is nonexistent. In our model, we defined this metal-semiconductor contact as Ohmic; nevertheless, we can observe the formation of a Schottky barrier with increasing interparticle distance. The magnitude of the interparticle spacing is directly related to the relative size of the low SBH region, which in this case, is an Ohmic region. As the interparticle distance doubles the size of the nanoparticles, a barrier forms with a magnitude of ca. one-fifth of the value of the high SBH region (i.e., SBH of the electrolyte interface). When the interparticle distance increases, the results showed a barrier height maximum of ca. two-thirds of the potential at the semiconductor-electrolyte junction (Figure 4D). The implications of this result may dictate that, even if the photocatalyst system presents an Ohmic junction with the active metallic sites, the electrolyte interface generates an energetic barrier for electron transfer around the hydrogen evolution site. This so-called pinch-off effect was first described by Tung for inhomogeneous metal-semiconductor Schottky contacts in solid-state devices; here, we observed the phenomena for the first time in particulate photocatalytic systems and propose that it may be detrimental for charge separation and transport. Figure 4E shows that the potential gradient under the semiconductor-electrolyte junction was affected in the presence of low barrier height regions if these Ohmic junctions are dense in the semiconductor surface. The potential profiles under the surface of the semiconductor were plotted in Figure 4F (gradient along the ρ-direction with x = 0.5 nm). The horizontal axis of the figures represents changing scales along the semiconductor surface with changing metal interparticle distance. Two extreme cases may be analyzed from the results presented in Figure 4F. When the nanoparticles in an Ohmic contact are isolated on the semiconductor surface, there are two well-defined potential regions with a steep potential gradient (-6 nm- red signal, Figure 4F). Nevertheless, with increasing interparticle distance, the potential minimum required for Ohmic behavior was not achieved below the surface. The potential gradient decreases with decreasing interparticle distance. If the nanoparticles are closely packed and the surface exposed to the electrolyte is

narrow, the potential gradient is almost non-existent (-1.5 nm-black signal, Figure 4F). The results imply that there would be an optimum interparticle distance at which the potential gradient extends sufficiently along the ρ-direction with an optimum electric field gradient for charge separation. The potential differences observed on both sides of Figure 4E may partially describe the charge separation mechanism used in heterogeneous single-absorber photocatalytic systems. Moreover, it may be the first glimpse of the origin of the low STH efficiency generally observed in particulate photocatalytic water splitting due to the limited charge separation probability of the system.[57,62]

Figure 5A and 5B show the equipotential profiles and carrier dynamics obtained for an n-type semiconductor decorated with a metallic catalyst in Ohmic contact with its surface following Model II and III, respectively. Figure 5A shows a single metal catalyst on the surface with a simplified box-type of geometry. The potentials were calculated relative to the semiconductor electron affinity on an absolute scale.

Columns represent models with changing properties (N_D, $\mu_{p,n}$, and $\tau_{p,n}$), and the rows qualitatively and quantitatively describe the electrostatics, charge transport vectors and carrier dynamics streamlines from top to bottom, respectively. Cones and arrows represent hole and electron drift-diffusion currents, respectively. Black and white streamlines were continuously drawn tangentially to the current vector field for holes and electrons, respectively. The donor density increases from left to right. For the calculations, we assumed that the mobility and lifetime of the carriers increases by one order of magnitude when the defect density decreases by similar proportions. The assumption of increasing lifetime and mobility as a function of decreasing carrier concentration were made following empirical observations in n-type and p-type Si and GaAs.[63–69] As expected, crystals with low defect densities showed wider depletion layers (>100 nm). A lower number of defects is generally considered beneficial for charge separation, and well-defined charge mobility profiles were observed from the results (Figure 5A, left).

10 | *J. Mater. Chem. A*, 2015, **00**, 1-3

This journal is © The Royal Society of Chemistry 2015
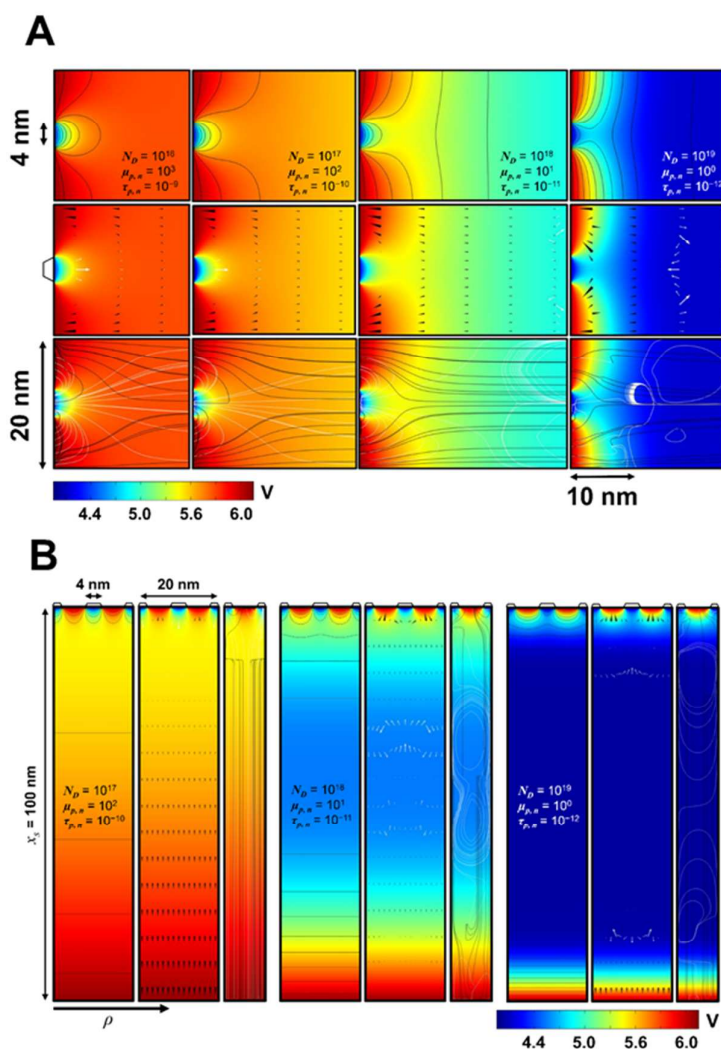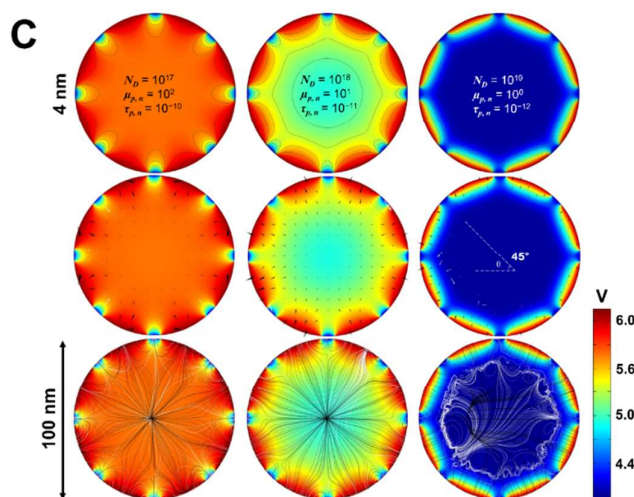
Fig. 5 Steady-state overall water splitting simulations for models under illumination conditions (Models II-IV). (A) Calculations for Model II were performed with a single 4-nm catalyst on the surface of an n-type semiconductor. For simplicity, only the results near the surface are shown in A; nevertheless, the model size is x = 100 nm into the bulk (A and B). (B) Calculations for Model I-III were obtained considering multiple particles on the surface of the semiconductor and an electrolyte interface on both sides of the model. (C) Model IV was used to obtained simulations for 100-nm semiconductor spherical particles with supported metal catalysts. Equipotential profiles are shown in the top row, current vectors in the middle row and streamlines for carriers transport in the bottom row (A and C). Donor density increases from left to right with the assumption of decreasing mobility and lifetime of the carriers. Metal contacts are assumed to be Ohmic whereas the electrolyte interface is assumed as a Schottky contact under water splitting conditions (E_g = 2.1 eV, χ = 4.3 eV, ε_r = 17, m^*_n = 1.9, m^*_h = 3.4, P_0 = 7×10^{20} m^{-2} s^{-1}).

The hole currents point towards the electrolyte interface, whereas opposite electron currents appeared under the metal-semiconductor Ohmic junction when defects are relatively low. As the donor density increases, the electrostatic profile of the depletion layer decreases to <10 nm and the recombination of carriers seems to increase (Figure 5A, N_D = 10^{19} cm^{-3}). At this point, electron currents are ill-defined and far from the Ohmic interface with the streamlines appearing to generate recombination pathways. Moreover, the directions of the electron current vectors were opposite, and with changing directions, which is another possible indication of charge recombination. Figure 5B presents the results obtained for Model III with multiple 4-nm nanoparticles on the semiconductor's surface. The size of the semiconductor slab is 100 nm. As described in the Model section, the metal nanoparticles on the top surface were assumed to produce Ohmic junctions under HER conditions. At the bottom of the figure, the surface is completely exposed to the electrolyte and

was assumed to be at the OER potential and to have a 300-mV overpotential. When the defect density is relatively low, we reasonably assumed a high carrier mobility and longer carrier lifetimes.[69] In contrast, when the donor density is high, we estimated that lifetime is on the order of picoseconds with a relatively low minority carrier mobility.[12] The results for Model III in Figure 5B were very similar to the ones observed in Figure 5A. Consistently, we observed the formation of large depletion regions with lower donor densities, whereas the potential gradient diminishes at the 10-nm scale with high carrier densities. Homogeneous and well-defined hole and electron currents were observed for donor densities lower than 10^{18} cm^{-3} with reasonable carrier pathways towards the electrolyte and the metal sites, respectively. With increasing donor density, charge recombination regions can be observed in Figure 5B. Current vectors for electrons presented opposite directions relative to the Ohmic site and streamlines formed random quasi-circular trajectories in the bulk of the

semiconductor. The chaotic electron and hole streamlines may represent recombination events in the semiconductor photocatalyst.

Figure 5C shows the results for Model IV with a catalyst size of 8 nm and an interparticle distance of approximately 39 nm. The photocatalyst donor density increases from left to right. We followed similar assumptions as before for mobility and lifetime. As the defect density decreases, the mobility and lifetime increase inversely proportional by one order of magnitude for the calculations. The photocatalyst size was assumed to be 100 nm based on literature reports.[17,19] The extents of the potential gradients decrease with increasing carrier density, as expected. No electric fields in the bulk were observed when the donor concentration was 10^{19} cm^{-3}. Under this condition, we assumed a lifetime on the order of picoseconds with a mobility of 1 cm^2 V^{-1} s^{-1} and, thus, a highly defective material. The solution of this system exhibited electron streamlines that do not reach the Ohmic site. The direction of the electron arrows for high carrier concentrations do not align with the metallic junction. The chaotic streamlines along with the ill-defined vectors may indicate higher recombination rates when using this parameters for a highly defective semiconductor. On the other extreme, if the donor concentration was below 10^{17} cm^{-3}, the current vectors homogeneously align with their respective carrier collecting sites. The electron and hole streamlines qualitatively show the charge generation and separation from almost any point in the bulk and surface when defects are low. The carriers flow into their respective active site sinks. Note that the size of streamlines, arrows and cones in the figure qualitatively describe the current transport and dynamics. The direction of the vectors accurately represents the calculation. The size and number of lines presented were arbitrarily selected to facilitate the visualization of the drift and diffusion results in these two-dimensional models.

Cut-lines were taken from the results shown in Figure 5B and 5C as shown in supplementary Figure S4A and S4B, respectively. Figure 6A shows the potential profiles obtained starting from the catalyst junction (i.e., Ohmic) and moving into the bulk towards the semiconductor-electrolyte backside interface (i.e., Schottky). A depletion region was observed in the rectifying junction as expected (Electrolyte interface, right side of Figure 6A). Consistent with the calculation results in Figure 4, a pinch-off effect was observed in the Ohmic side at high donor concentrations of $>10^{18}$ cm^{-3}. Such an energetic barrier may be detrimental for electron injection into the hydrogen active site. This pinch-off effect may originate from the electrostatic influence of the electrolyte surrounding the metal site. The potential wells observed in Figure 6A and 6B may contribute to an increase in the carrier's recombination rate, thus decreasing the efficiency (see below). As the carrier density decreases, it was possible to observe a charging effect in the bulk of the semiconductor. Decreasing the amount of defects in the semiconductor along with increasing mobility and lifetime of the carriers, generated a potential profile across the absorber particle that seems appropriate for efficient charge separation (Figure 6A, 10^{16} cm^{-3}). The results

are consistent with the report by Hisatomi et al. using a one-dimensional model and assuming a so-called asymmetric photocatalytic geometric model.[42] Figure 6B exhibits similar potential profiles now obtained from Model IV using the cut-line shown on Figure S4B. The plot describes the potential gradient under the metal site across the spherical semiconductor particle into another Ohmic region on the surface of the photocatalyst model. In this case, both sides of the junction are in Ohmic contact, and the pinch-off effect can be observed at both ends of Figure 6B. Similar conclusions can be drawn from the models. The potential wells in the bulk may promote charge recombination ($>10^{18}$ cm^{-3}), and the electrolyte can inhibit electron transfer into the metallic site due to the formation of a barrier resulting from the pinch-off effect.
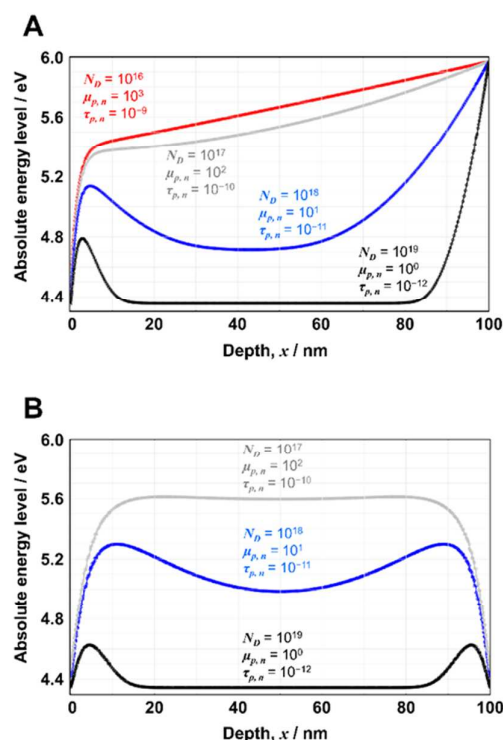
Fig. 6 Absolute energy levels as a function of distance into the semiconductor bulk as obtained from cut-lines drawn in the results presented in (A) Figure 5B and (B) Figure 5C. The one-dimensional profiles are taken as illustrated in the supplementary Figure S4. The energy profile is calculated under the catalyst, into the semiconductor bulk, towards the opposite electrolyte interface (A – Model III). The potential gradient is presented from one of the catalysts, into the semiconductor bulk, towards another metal nanoparticle in the surface of the semiconductor model (B – Model IV).

12 | *J. Mater. Chem. A*, 2015, **00**, 1-3

This journal is © The Royal Society of Chemistry 2015

ARTICLE

The calculated current densities at the Schottky and Ohmic interfaces were used to estimate the amount of carriers available for redox reactions. Assuming that each photon generates an electron-hole pair, we estimated a local QE per absorbing particle by calculating the ratio between incident photons from the solar spectrum (AM 1.5G) and the number of usable charge carriers at the two different terminals in this model, i.e., the Schottky and Ohmic junctions. Figure 7A shows the QE of one particle as a function of the donor density as well as the changing carrier mobility and lifetime. The QE increases with decreasing donor density, reaching a maximum plateau of 45% at $\leq 10^{17}$ cm^{-3} for Models II, III and I-III. Using Model IV we calculated a theoretical maximum QE of 35.7% for a single absorbing unit. As the carrier density increases the QE decreases, most likely due to the increasing recombination rates as observed from the results in Figure 5. We can reasonably speculate that the observed formation of potential wells in the semiconductor bulk along with the pinch-off effect contributed to the calculated low QE. For defective semiconductor powders, we calculated a low QE of <10% for a single absorbing unit. The cross and star symbols in the data in Figure 7 represents the results when a longer lifetime was used for the calculations, as described in the figure. Although it was observed that the calculated QE at high donor densities roughly doubles in magnitude when τ increases in one order of magnitude; there was a clear plateau around a QE of 35% (Figure 7A, single absorbing unit). It is interesting to note that, by increasing the lifetime by one order of magnitude, it was possible to achieve the maximum QE for the configuration at a relatively high donor concentration of 10^{18} cm^{-3}. Moreover, all models used in these calculations resulted in a very similar trends for QE, as observed in Figure 7. We also confirmed that increasing the lifetime of the carriers to hundreds of picosecond or longer saturates the attainable QE to the maximum values calculated and presented in this Figure (35%), even under high carrier concentrations $\geq 10^{18}$ cm^{-3}. In contrast to the theoretical values reported in the literature,[42] it was not possible to obtain a QE larger than 50% for a single unit using this typical metal-supported semiconductor photocatalyst configuration.

Figure 7B presents the calculations for the accumulated quantum efficiency (AQE) for four consecutive particles as a function of changing properties of the semiconductor. The STH efficiency was plotted in the figure by taking the AQE and computing the attainable hydrogen production efficiency if simulated sunlight was used. After four successive particles, AQE efficiencies larger than 90% were observed when the carrier concentration was relatively small. When Model IV was employed for the calculations, the maximum ideal AQE was approximately 70%. At high donor densities, most of the models resulted in AQE of less than 10%, except for Model IV, that generated 18% AQE. The same trends are reflected in the attainable STH. Solar-to-hydrogen efficiencies decrease with increasing carrier densities with a maximum of 12.6% and a minimum of ca. 1%. As mentioned earlier, the star symbol in the data represents the assumption of a larger lifetime of the

carriers (Figure 7B). Ideally and under this set of assumptions, it was possible to observe 10% STH for a semiconductor with a relatively high donor density of 10^{18} cm^{-3} and 5% STH for 10^{19} cm^{-3}; only if it is possible to increase the carrier lifetime by one order of magnitude under this defective conditions (i.e. larger than hundredths of picoseconds).

To further test the effect of the interparticle distance of the catalyst and the catalyst size on the QE of the system, we used our calculations on Model IV to emulate a more complex photocatalyst. We modelled a 100-nm semiconductor particle using the reported properties for n-type Ta$_3$N$_5$ materials.[12,13,17,19] We decorated the surface of the semiconductor with nanoparticles of different sizes separated by a changing interparticle distance (Figure 8A). The angle determines the interparticle distance: a 30° angle results in approximately 26 nm, 45° results in approximately 39 nm and a 90° angle isolates the metals at a distance of approximately 79 nm. Figure 8A exhibits three representative metal nanoparticle sizes of 1, 8 and 20 nm in diameter assuming a hemispherical particle supported on the

This journal is © The Royal Society of Chemistry 2015

J. Mater. Chem. A, 2015, **00**, 1-3 | **13**
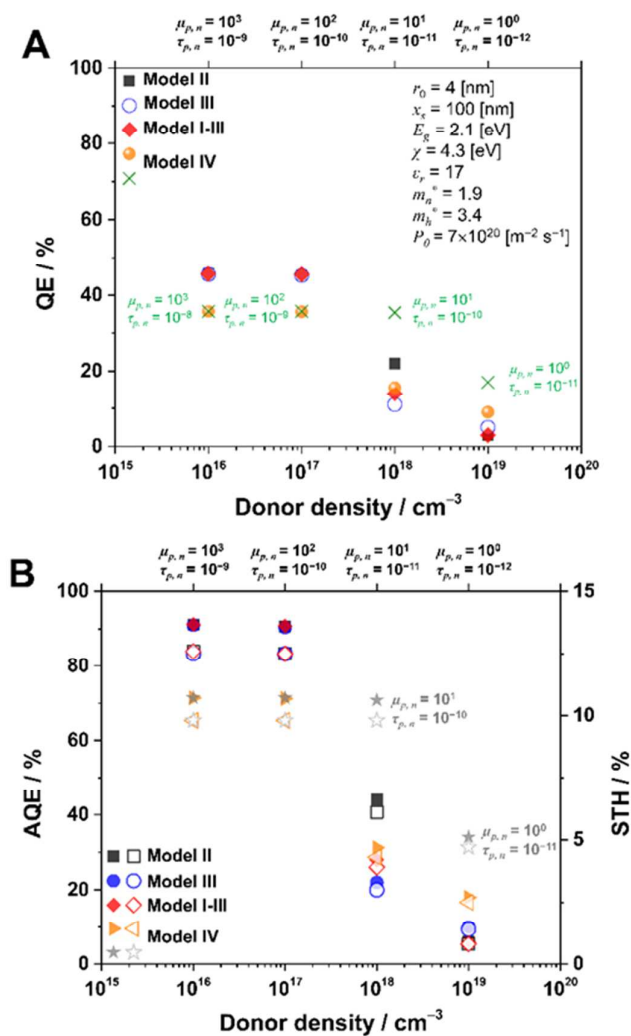
Fig. 7 (A) Quantum efficiency of a single 100-nm n-type semiconductor as a function of donor density. (B) Accumulated quantum efficiency (AQE, filled symbols, left y-axis) and solar-to-hydrogen efficiency (open symbols, right y-axis) as a function of donor density calculated after four particles. It was assumed that charge carrier mobility and lifetime increase with decreasing carrier density. The calculated quantum efficiency was obtained from the Models presented in Figure 5 under steady-state conditions for redox reactions under illumination. STH was calculated from simulated solar radiation AM 1.5G for Ta_3N_5 (300 nm < λ < 500 nm).

semiconductor surface. In an effort to model a realistic defective particulate semiconductor photocatalyst, we used a donor density of 10^{19} cm^{-3}, an experimentally measured lifetime of 5 ps and an electron mobility of 2 cm^2 V^{-1} s^{-1}.[12] In this calculation, we assumed that the hole mobility was 1 order of magnitude lower than the electron mobility, based on the reported calculations of the effective masses.[13] Figure 8B shows the calculated QE and AQE as a function of the catalyst particle size with changing the interparticle distance on the semiconductor surface. It is interesting to note that the maximum attainable efficiency under these parameters was
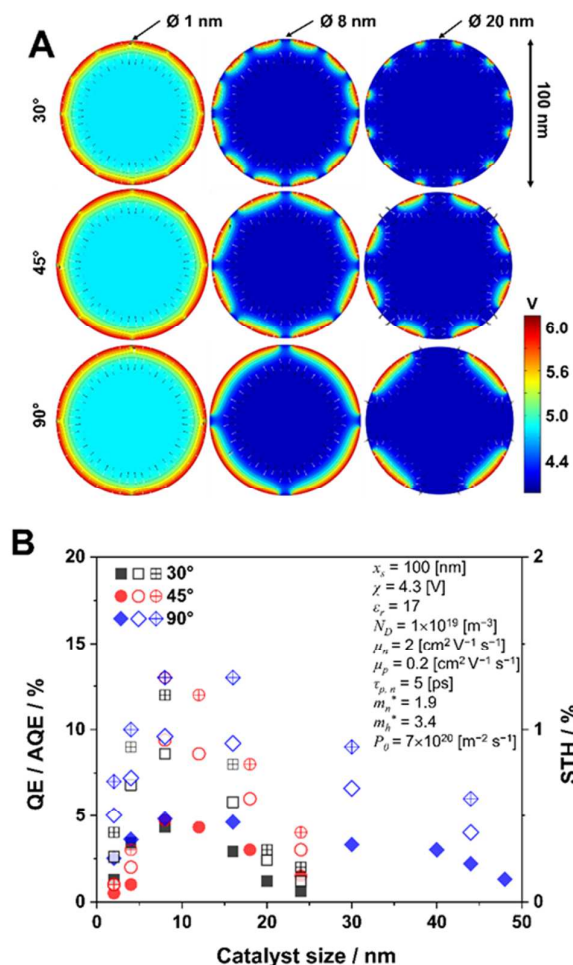
Fig. 8 Simulations using Model IV with different dispersion and size of the catalysts on the surface of a 100-nm *n*-type semiconductor. The rows show a changing interparticle distance and the columns show a different catalyst size (A). Quantum efficiency (filled symbols) and accumulated QE (open symbols) after four consecutive units as a function of the catalyst size with varied interparticle distance (B). Solar-to-hydrogen efficiency is shown on the left axis and was calculated from AM 1.5G using the simulation results for QE (B, crossed symbols). Typical properties of Ta_3N_5 powders were considered for the calculations (E_g = 2.1 eV, χ = 4.3 eV, ε_r = 17, m^*_n = 1.9, m^*_h = 3.4, μ_n = 2 cm^2 V^{-1} s^{-1}, μ_p = 0.2 cm^2 V^{-1} s^{-1}, $\tau_{p,n}$ = 5 ps, P_0 = 7×10^{20} m^{-2} s^{-1}).

≤5% QE for a single absorbing unit; such efficiency translates to a maximum of approximately 10% AQE (1.3% STH, AM 1.5G, 300 nm < λ < 500 nm). As the interparticle distance decreased, the optimal particle size for maximum QE had a narrower distribution. Although, there was a minor interparticle distance effect, it was possible to find an efficiency maxima for approximately 8-12 nm catalyst particles. This result must be considered carefully because the size of the catalyst strongly influences the kinetics of electrocatalytic water reduction (and oxidation), which significantly defines the overall STH efficiency of the real photocatalytic system.[19] Nevertheless, the observed maxima may imply that the metal-semiconductor junction size plays a role in charge separation and was consistent with the results from Figure 3 and 4. Hence, the electrocatalyst-semiconductor interface must be thoroughly considered when designing new photocatalytic systems.

The developed numerical modeling enabled us to randomly and individually perturb the semiconductor parameters to measure the effects on the overall photocatalytic quantum efficiency within the constraints. Quantitatively, it was possible to obtain 45% QE for one particle if the semiconductor donor density is ≤10^{18} cm^{-3} (Figure 7A). The latter may be technologically challenging in the synthesis of particulate photocatalysts.[48] Nevertheless, multiple absorbing entities in the slurry ideally increases the total achievable QE. Indeed, as previously mentioned, one of the advantages of particulate photocatalytic water splitting is the use of multiple absorbing entities suspended in solution. We confirmed that the local charge transport efficiency remains almost constant with light decay up to approximately 4 consecutive particles in the size range of 100 nm. If we take the lowest boundary of 5% QE per absorbing unit (Figure 7A and 8B), the AQE after four particles reached approximately 10% before a significant efficiency decay was observed. While still low for an ideal system, the calculations indicate that it is still possible to increase to approximately 91% AQE after four consecutive semiconductor particles if a single absorbing unit exhibits a QE of approximately 45% corresponding to 12.6% STH for a model Ta_3N_5 photocatalyst absorbing 300 nm < λ < 550 nm in AM 1.5G (Models II, III and I-III). Nevertheless, the calculations for Model IV exhibited a maximum of ca. 71% AQE under the most favorable parameters (9.8% STH, AM 1.5G, 300 nm < λ < 500 nm).

14 | *J. Mater. Chem. A*, 2015, **00**, 1-3

This journal is © The Royal Society of Chemistry 2015

When taking the lower threshold of the calculations, a single absorbing element, consuming photons from UV to 550 nm with a 20% QE, may achieve a 40% AQE after four particles; representing an STH of approximately 5.5%, which may become economically competitive.[1] Nevertheless, the calculated low-efficiency trends in this ideal model reflect the intrinsic limitations of the ordinary photocatalytic particle.

Conclusions

Using simplified simulations of semiconductor devices, crucial properties were identified in metal-supported semiconductor photocatalysts to achieve a basic design for efficient water splitting. In this simulation, the metal as the electrocatalyst on the surface is an integral and vital component in this system to provide anisotropic electronic field within the semiconductor for effective charge separation (and to enhance the kinetics of the redox reactions which were omitted from the simulation). From the knowledge gained from the calculations, we however suggest that the classic photocatalytic design with random dispersion of metal nanoparticles on a semiconductor absorber does not improve the efficiency; on the contrary, it may be even hindering the overall development of the system. Future particulate photocatalysts must create an effective path for the transport of electrons and holes into their respective active sites. The semiconductor-electrolyte interface may be one of the major contributors for charge separation; however, as illustrated in this study, the depletion layer of this interface generates a pinch-off effect, directly affecting electron transport into the hydrogen evolution sites due to Schottky barrier formation. Moreover, the potential gradients observed for charge separation were only present near the semiconductor surface with very limited and constrained space regions (<10 nm, in defective semiconductor powders). Hence, inefficient charge separation in the bulk limits the efficiency, because most of the generated electron-hole pairs from sunlight's long-wavelength photons are created in the bulk and far from the charge collection region. The trends obtained clearly exhibited an intrinsic limitation of the typical photocatalytic configuration. In the best case scenario, it was only possible to achieve less than half of the ideal QE for a single absorber. Novel synthetic strategies are required, and nanostructuring of the photocatalysts may provide a first step to improving efficiencies. Other than decreasing the semiconductor size to introduce quantum-confinement effects, a photon collection strategy must be implemented to harvest the visible light region of the solar spectrum efficiently without compromising the charge collection probability. More importantly, we must rigorously design the majority carrier pathway that is, in general, inhibited by the electrolyte junction. One of such strategies may be to use a metal-insulator-semiconductor type junction or a carefully embedded buried-junction active-site electronically isolated from environmental effects. To achieve a breakthrough, the objective must be to control the charge carrier injection into the kinetically active electrocatalyst using a photocatalysis by design strategy in contrast to a black-box catalysis approach.

Acknowledgements

References

1   K. Takanabe and K. Domen, *Green*, 2011, **1**, 313–322.
2   J. R. McKone, N. S. Lewis, and H. B. Gray, *Chem. Mater.*, 2014, **26**, 407–414.
3   A. Fujishima and K. Honda, *Nature*, 1972, **238**, 37–38.
4   M. G. Walter, E. L. Warren, J. R. McKone, S. W. Boettcher, Q. Mi, E. a Santori, and N. S. Lewis, *Chem. Rev.*, 2010, **110**, 6446–73.
5   J. Schneider, M. Matsuoka, M. Takeuchi, J. Zhang, Y. Horiuchi, M. Anpo, and D. W. Bahnemann, *Chem. Rev.*, 2014, **114**, 140919080959008.
6   A. L. Linsebigler, G. Lu, and J. T. Yates, *Chem. Rev.*, 1995, **95**, 735–758.
7   A. Kudo and Y. Miseki, *Chem. Soc. Rev.*, 2009, **38**, 253–78.
8   K. Takanabe, in *Topics in current chemistry*, Springer Berlin Heidelberg, 2015.
9   B. Ohtani, *Chem. Lett.*, 2008, **37**, 216–229.
10 T. Hisatomi, K. Takanabe, and K. Domen, *Catal. Letters*, 2014, **145**, 95–108.
11 M. Harb, P. Sautet, E. Nurlaela, P. Raybaud, L. Cavallo, K. Domen, J.-M. Basset, and K. Takanabe, *Phys. Chem. Chem. Phys.*, 2014, **16**, 20548–60.
12 A. Ziani, E. Nurlaela, D. S. Dhawale, D. A. Silva, E. Alarousu, O. F. Mohammed, and K. Takanabe, *Phys. Chem. Chem. Phys.*, 2015, **17**, 2670–7.
13 E. Nurlaela, M. Harb, S. del Gobbo, M. Vashishta, and K. Takanabe, *J. Solid State Chem.*, 2015, **229**, 219–227.
14 A. T. Garcia-Esparza, D. Cha, Y. Ou, J. Kubota, K. Domen, and K. Takanabe, *ChemSusChem*, 2013, **6**, 168–81.
15 T. Shinagawa, A. T. Garcia-Esparza, and K. Takanabe, *ChemElectroChem*, 2014, **1**, 1497–1507.
16 T. Shinagawa and K. Takanabe, *J. Phys. Chem. C*, 2015, 150824091143002.
17 E. Nurlaela, S. Ould-Chikh, M. Harb, S. del Gobbo, M. Aouine, E. Puzenat, P. Sautet, K. Domen, J.-M. Basset, and K. Takanabe, *Chem. Mater.*, 2014, **26**, 4812–4825.
18 W. Yu, T. Isimjan, S. Del Gobbo, D. H. Anjum, S. Abdel-Azeim, L. Cavallo, A. T. Garcia-Esparza, K. Domen, W. Xu, and K. Takanabe, *ChemSusChem*, 2014, **7**, 2575–83.
19 E. Nurlaela, S. Ould-Chikh, I. Llorens, J.-L. Hazemann, and K. Takanabe, *Chem. Mater.*, 2015, **27**, 5685–5694.
20 Z. Chen, T. F. Jaramillo, T. G. Deutsch, A. Kleiman-Shwarsctein, A. J. Forman, N. Gaillard, R. Garland, K. Takanabe, C. Heske, M. Sunkara, E. W. McFarland, K. Domen, E. L. Miller, J. a. Turner, and H. N. Dinh, *J. Mater. Res.*, 2011, **25**, 3–16.
21 X. Chen, S. Shen, L. Guo, and S. S. Mao, *Chem. Rev.*, 2010, **110**, 6503–70.
22 H. Kisch, *Angew. Chem. Int. Ed. Engl.*, 2013, **52**, 812–47.
23 R. Marschall, *Adv. Funct. Mater.*, 2013, n/a–n/a.
24 J. B. Baxter, C. Richter, and C. A. Schmuttenmaer, *Annu. Rev. Phys. Chem.*, 2014, **65**, 423–47.
25 T. Hisatomi, J. Kubota, and K. Domen, *Chem. Soc. Rev.*, 2014, **43**, 7520–7535.
26 W. J. Albery, *J. Electrochem. Soc.*, 1984, **131**, 315.
27 Z. Zhang and J. T. Yates, *Chem. Rev.*, 2012, **112**, 5520–51.
28 J. A. Turner, *J. Chem. Educ.*, 1983, **60**, 327.

Journal of Materials Chemistry A Accepted Manuscript

29 M. Grätzel, *Nature*, 2001, **414**, 338–344.
30 K. Rajeshwar, in *Encyclopedia of Electrochemistry*, ed. A. J. Bard, Wiley-VCH Verlag GmbH & Co. KGaA, Weinheim, Germany, 2007.
31 R. C. Rossi and N. S. Lewis, *J. Phys. Chem. B*, 2001, **105**, 12303–12318.
32 R. C. Rossi, M. X. Tan, and N. S. Lewis, *Appl. Phys. Lett.*, 2000, **77**, 2698.
33 F. Lin and S. W. Boettcher, *Nat. Mater.*, 2014, **13**, 81–6.
34 T. J. Mills, F. Lin, and S. W. Boettcher, *Phys. Rev. Lett.*, 2014, **112**, 148304.
35 J. Bisquert, P. Cendula, L. Bertoluzzi, and S. Gimenez, *J. Phys. Chem. Lett.*, 2014, **5**, 205–207.
36 P. Cendula, S. D. Tilley, S. Gimenez, J. Bisquert, M. Schmid, M. Grätzel, and J. O. Schumacher, *J. Phys. Chem. C*, 2014, **118**, 29599–29607.
37 H. Gerischer, *J. Phys. Chem.*, 1984, **88**, 6096–6097.
38 Y. Nosaka, K. Norimatsu, and H. Miyama, *Chem. Phys. Lett.*, 1984, **106**, 128–131.
39 J. S. Curran, J. Domenech, N. Jaffrezic-Renault, and R. Philippe, *J. Phys. Chem.*, 1985, **89**, 957–963.
40 Y. Nosaka, Y. Ishizuka, and H. Miyama, *Berichte der Bunsengesellschaft für Phys. Chemie*, 1986, **90**, 1199–1204.
41 T. Ioannides and X. Verykios, *J. Catal.*, 1996, **569**, 560–569.
42 T. Hisatomi, T. Minegishi, and K. Domen, *Bull. Chem. Soc. Jpn.*, 2012, **85**, 647–655.
43 S. M. Sze and K. Ng, *Physics of Semiconductor Devices*, John Wiley & Sons Inc., 3rd Ed., 2007.
44 R. Entner, PhD thesis, Technischen Universitat Wien, 2007.
45 M. Schiavello, *Photoelectrochemistry, Photocatalysis and Photoreactors*, Springer Netherlands, Dordrecht, 1985.
46 K. Takanabe and K. Domen, in *Heterogeneous Catalysis at Nanoscale for Energy Applications*, eds. F. F. Tao, W. F. Schneider, and P. V. Kamat, John Wiley & Sons, Inc, Hoboken, NJ, 2014.
47 Z. Zhang and J. T. Yates, *Chem. Rev.*, 2012, **112**, 5520–51.
48 K. Takanabe and K. Domen, *ChemCatChem*, 2012, **4**, 1485–1497.
49 Y. Li, L. Zhang, A. Torres-Pardo, J. M. González-Calbet, Y. Ma, P. Oleynikov, O. Terasaki, S. Asahina, M. Shima, D. Cha, L. Zhao, K. Takanabe, J. Kubota, and K. Domen, *Nat. Commun.*, 2013, **4**, 2566.
50 M. Dou and C. Persson, *Phys. status solidi*, 2012, **209**, 75–78.
51 M. Huda, Y. Yan, S.-H. Wei, and M. Al-Jassim, *Phys. Rev. B*, 2008, **78**, 195204.
52 Y. Wang and N. Herron, *J. Phys. Chem.*, 1987, **91**, 257–260.
53 W. W. Yu, L. Qu, W. Guo, and X. Peng, *Chem. Mater.*, 2003, **15**, 2854–2860.
54 M. Cohen and R. Blunt, *Phys. Rev.*, 1968, **168**, 929–933.
55 C. Lee, J. Destry, and J. Brebner, *Phys. Rev. B*, 1975, **11**, 2299–2310.
56 K. Maeda and K. Domen, *J. Phys. Chem. Lett.*, 2010, **1**, 2655–2661.
57 K. Maeda, K. Teramura, D. Lu, T. Takata, N. Saito, Y. Inoue, and K. Domen, *Nature*, 2006, **440**, 295.
58 R. T. Tung, *Appl. Phys. Rev.*, 2014, **1**, 011304.
59 R. T. Tung, *Phys. Rev. B*, 1992, **45**, 13509–13523.
60 R. T. Tung, *Appl. Phys. Lett.*, 1991, **58**, 2821.
61 J. P. Sullivan, R. T. Tung, M. R. Pinto, and W. R. Graham, *J. Appl. Phys.*, 1991, **70**, 7403.
62 C. Pan, T. Takata, M. Nakabayashi, T. Matsumoto, N. Shibata, Y. Ikuhara, and K. Domen, *Angew. Chem. Int. Ed. Engl.*, 2015, **54**, 2955–9.
63 H. Ito, T. Furuta, and T. Ishibashi, *Appl. Phys. Lett.*, 1991, **58**, 2936.
64 H. C. Casey, *J. Appl. Phys.*, 1973, **44**, 1281.

65 S. E. Swirhun, Y.-H. Kwark, and R. M. Swanson, in *1986 International Electron Devices Meeting*, IRE, 1986, vol. 32, pp. 24–27.
66 S. E. Swirhun, J. A. del Alamo, and R. M. Swanson, *IEEE Electron Device Lett.*, 1986, **7**, 168–171.
67 J. A. del Alamo and R. M. Swanson, *IEEE Trans. Electron Devices*, 1987, **34**, 1580–1589.
68 M. S. Tyagi and A. K. Gupta, *Phys. Status Solidi*, 1994, **143**, 79–83.
69 M. E. Law, E. Solley, M. Liang, and D. E. Burk, *IEEE Electron Device Lett.*, 1991, **12**, 401–403.

Journal of Materials Chemistry A Accepted Manuscript

A guideline to achieve efficient photocatalytic water splitting is presented using theoretical simulations of particulate semiconductors decorated with metal particles.